American Mineralogist, Volume 110, pages 1728–1736, 2025

Nanoscale mapping of $ZrSiO_4$ phases in naturally shocked zircon using electron energy loss spectroscopy

Vladimir Roddatis[1,*,§], Elizaveta Kovaleva[1,2,3,†], Marcin D. Syczewski[1,‡], Anja Schreiber[1], and Richard Wirth[1]

[1]GFZ Helmholtz Centre for Geosciences, Telegrafenberg, 14473 Potsdam, Germany
[2]Department of Earth Sciences, University of the Western Cape, Robert Sobukwe Road, 7535 Bellville, South Africa
[3]Department of Geological Sciences, School of Agricultural, Earth and Environmental Sciences, University of KwaZulu-Natal, Private Bag, Westville, X54001, South Africa

Abstract

Coexistence in natural samples of zircon ($ZrSiO_4$) and reidite (a high-pressure polymorph of $ZrSiO_4$) is attributed to the effects of hypervelocity impact events. The grains and intergrowths in those minerals can be merely a few nanometers in size, which makes phase identification by standard methods of structure analysis difficult. However, analytical scanning transmission electron microscopy (STEM) utilizing electron energy loss spectroscopy (EELS) can provide important information on phase transition mechanisms and pressure-temperature conditions associated with the shock event at the nanoscale. Here we demonstrate that the valence as well as oxygen core-loss EELS can be employed for nanoscale mapping of zircon-reidite distributions in zircon-reidite aggregates. Moreover, other accompanying phases, e.g., baddeleyite, could also be identified and mapped by this method. We further compare the EELS maps with a 4D-STEM nanobeam precession electron diffraction data, and demonstrate the advantages of the EELS mapping, which provides spatial resolution down to the nanometer scale and is independent of crystal orientation.

Keywords: Zircon, reidite, EELS, phase mapping, Kara impact structure

Introduction

The natural occurrence of reidite, the high-pressure phase of zircon ($ZrSiO_4$), is regarded as one of the criteria for shock metamorphism (Reddy et al. 2015). However, the mechanism and exact *P-T-t* conditions of the zircon-reidite phase transition remain unclear (Erickson et al. 2017; Mihailova et al. 2019). In natural and synthetic samples, the presence of reidite has been confirmed by: X-ray powder diffraction (Kusaba et al. 1985; Knittle and Williams 1993; Glass et al. 2002); Raman and infrared spectroscopy (Gucsik et al. 2002, 2004; Wittmann et al. 2006); and electron diffraction patterns in transmission electron microscopy (TEM) (Leroux et al. 1999). In the last 10 years, the most common method to detect reidite has relied on a combination of scanning electron microscopy (SEM) backscattered electron (BSE) imaging, energy-dispersive spectroscopy (EDS) analyses, and electron backscattered diffraction (EBSD) (Reddy et al. 2015; Erickson et al. 2017; Xing et al. 2020; Plan et al. 2021; Zhao et al. 2024).

However, SEM imaging, EBSD mapping and Raman spectroscopy do not provide a spatial resolution high enough to access the complexity of the impact-produced Zr-phases, their reaction products and deformation microstructures (Kovaleva et al. 2021, 2023). Mineral grains and intergrowths in such samples can be as small as a few nanometers in size and thus below the resolution of SEM imaging (Kovaleva et al. 2021; Zhao et al. 2024) and Raman spectroscopy (Wittmann et al. 2006), which is a serious limitation leading to imprecise interpretations of processes. This problem was highlighted by Wittmann et al. (2006), who suspected the presence of an orthorhombic-II (OII) polymorph of ZrO_2 in impact glasses, but could not conclusively confirm it with Raman spectroscopy.

On the other hand, electron energy loss spectroscopy (EELS) in combination with scanning TEM (STEM) is a powerful tool used to extract important information in materials science (Colliex 2022). EELS chemical mapping is routinely employed to visualize phase and element distribution down to the atomic scale (Mundet et al. 2021; Yeh et al. 2023). Moreover, EELS is capable of distinguishing allotropes of carbon based on their fine *K*-edge structure (Egerton et al. 1974). Generally, the low energy or valence region of EELS (VEELS) is utilized to measure band gaps in materials and to map the distribution of phases in hard and soft materials (Chen et al. 2024; Mu et al. 2016; Badr et al. 2023; Liang et al. 2018; Rossner et al. 2018). At the same time, the comprehensive interpretation of VEELS regions is very complicated, because they include various collective excitations (plasmons) as well as inner- and intraband transitions (Egerton 1996).

In this paper, we compare the VEELS and core-loss regions of reidite and zircon spectra and use them to visualize the nanoscale distribution of $ZrSiO_4$ phases in naturally shocked zircon grains from the Kara impact structure located in polar Russia. We document a simple and fast method of micro- and nanophase identification with very high spatial resolution using STEM. Using the obtained high-resolution data, we are improving constraints on the phase transition mechanism and impact conditions. The presented workflow can also be applied to any other geological samples with nanoscale textures and grain sizes for phase identification and mapping with very high spatial resolution.

* Corresponding author E-mail: roddatis@gfz-potsdam.de Orcid https://orcid.org/0000-0002-9584-0808
† Orcid https://orcid.org/0000-0002-3221-3444
‡ Orcid https://orcid.org/0000-0001-6434-3027
§ Open access. Article available to all readers online under the following license terms: CC BY.

0003-004X/25/0011–1728$05.00/DOI: https://doi.org/10.2138/am-2024-9455

Materials and Methods

Materials

The 65 km diameter, 70.3 Ma Kara impact structure (Trieloff et al. 1998) (Fig. 1a) is located in the Yugorsky Peninsula, Russia. The target rocks of the Kara structure are a folded terrigenous and carbonate Upper Proterozoic to Paleozoic sedimentary sequence, with the Ordovician-Carboniferous and early Permian sedimentary rocks topping the sequence (Masaitis 1999). Massive lithic breccias are overlain by allogenic suevites and impact melt rocks (tagamites). Suevites are composed of sandstone, limestone and slate, glass bombs, and veins, embedded in the fine-grained crushed matrix. Samples were collected from the crater-infill suevite breccias. Sample KK21-21 (GPS: 68°54′07.8″N 64°33′48.2″E) is a gray suevite in contact with the bedrock limestone (Fig. 1b). Sample KH21-08 (GPS: 68° 56′50.9″N 64°50′26.8″E) is a brown suevite with large fluidal-textured glass fragments (Fig. 1c). Foil #7081 is from irregular zircon grain hosted by the fine-grained clastic matrix of a lithic fragment, likely a poorly sorted sandstone (sample KK21-21). The grain has characteristic subparallel short fractures and <1 μm thick reidite inclusions (bright in BSE). Reidite forms two sets of parallel lamellae and an irregular network of thinner veinlets (Fig. 1d). Foil #7103 is from subhedral zircon embedded into a lithic clast that resembles weakly foliated slate (sample KK21-08). Zircon has patchy flame-shaped inclusions of reidite in the core (BSE-bright) and radial fractures in the rim (Fig. 1e). Foil #7080 is from an aggregate at the boundary between a sandstone clast and fine-grained glass-rich matrix (sample KK21-21, Online Materials[1] Fig. SI1). The aggregate has a porous texture and is composed of two fragments with radiating spherulitic internal texture (Fig. 1f).

Methods

TEM foils of approximately 15 × 10 μm were prepared by a lift-out method using a focused ion beam (FIB) Thermo Fisher Scientific (TFS) Helios G4UC instrument. TEM experiments were done using a TFS Themis Z 80-300 (S) TEM operated at 300 kV, and equipped with a TFS SuperX Energy-dispersive X-ray (EDX) detector, and a Gatan Imaging Filter (GIF) Continuum 1065. The individual reference EELS spectra and spectrum images (SIs) of studied specimens were collected with 0.15 and 1.5 eV dispersion using a Gatan Microscopy Suite (GMS or DigitalMicrograph) software. Using the Fourier-log ratios, the estimated specimen thickness in terms of the effective mean-free path (λ_{eff}) for inelastic scattering was ~0.7 and, based on the Kramers-Kronig analysis (Kronig 1926;

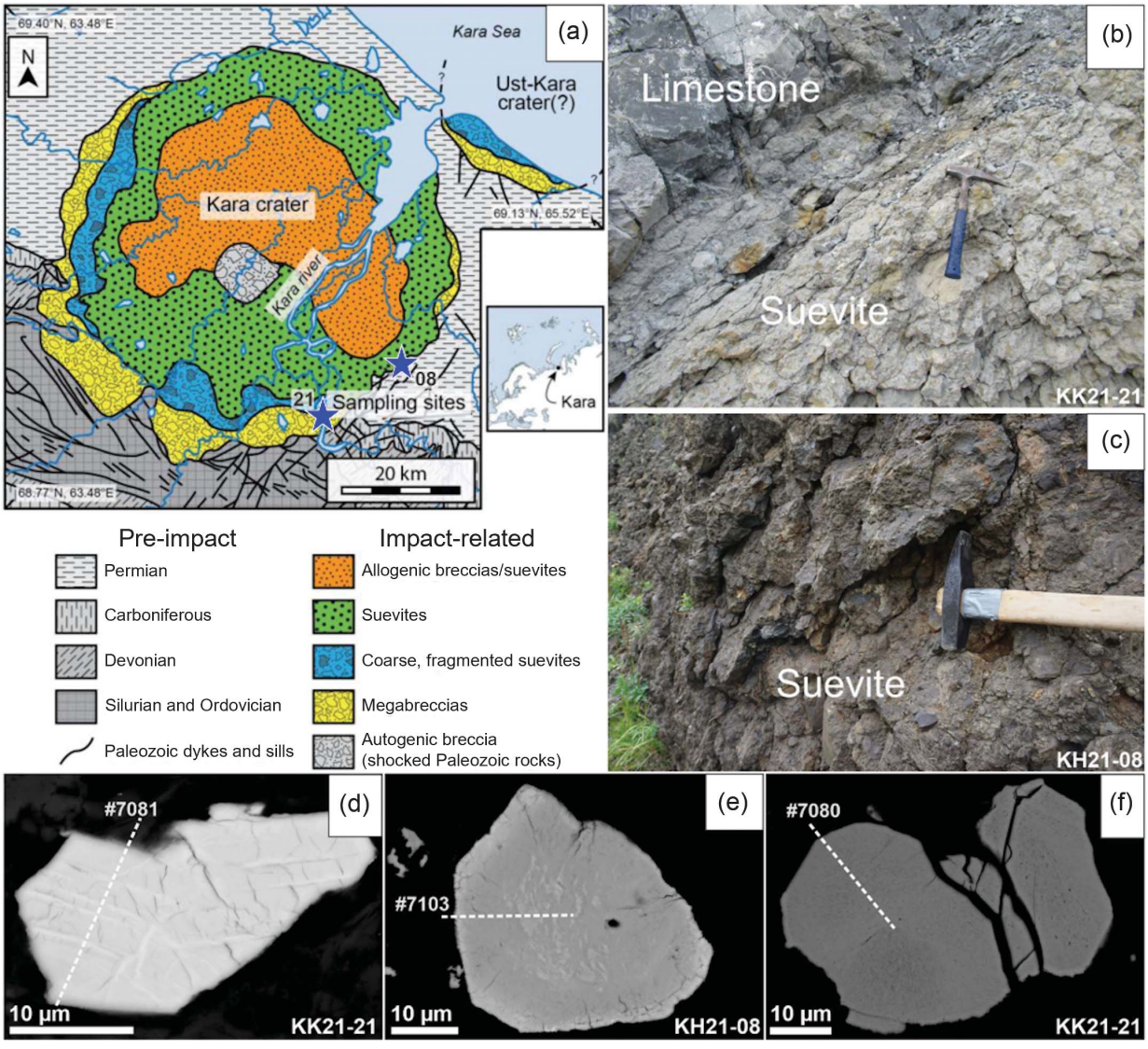

Figure 1. (**a**) Schematic geological map of Kara impact structure from Kenny et al. (2021). Blue stars indicate sampling locations from the crater rim. (**b**–**c**) Field photographs of the sampled outcrops. In (**b**), light yellow-gray suevite intercalates with the blocks of gray shattered limestone. (**d**–**f**) BSE images of studied $ZrSiO_4$ aggregates. The broken lines indicate the positions from which the TEM samples were cut.

Kramers 1927), corresponds to an approximately 70 nm FIB foil thickness. Collected reference EELS spectra of zircon and reidite with their characteristic features were subjected to zero-loss peak fitting with Gaussian-Lorentz functions, followed by deconvolution and background subtraction (Johnson and Spence 1974), using the GMS built-in functions. The reference spectra prepared this way were used for multiple linear least-squares (MLLS) fitting (Leapman and Swyt 1988; Yakovlev and Libera 2008) of individual EELS spectra from the corresponding SIs to visualize the distribution of phases in the TEM specimens. The GMS software features a built-in routine for performing MLLS fitting within a specified energy range (e.g., 10–60 eV). Electron diffraction data were collected and analyzed using a precession electron diffraction (PED) DigiSTAR device and the ASTAR software (NanoMEGAS SPRL, Belgium). The pole figures were prepared with an EDAX OIM Analysis software.

Results

In the high-angle annular dark-field (HAADF) image (Fig. 2a), reidite forms sets of thin lamellae inside fractured zircon. The EDX chemical maps indicate the absence of other phases (Online Materials[1] Fig. SI2). Zircon and reidite were also identified using selected area electron diffraction (SAED). The SAED pattern of reidite in [110] zone axis orientation shows multiple forbidden spots and broadening of high order with asterism, which indicates a high density of defects and structural disorder of the reidite lamellae (Fig. 2b).

The positions and shapes of VEELS peaks of both phases are almost independent of the specimen orientation with respect to the incident electron beam (Fig. 2d; Online Materials[1] Fig. SI3). The VEELS of zircon is consistent with previously reported spectra (Jiang and Spence 2013). Zircon and reidite have distinct VEELS spectra (Fig. 2d), namely the largest peak at 25.5 eV associated with bulk plasmon in zircon is shifted by 2.3 to 27.6 eV in reidite. Other spectrum features are much less different. For example, a bump at around 8.0 eV is present in spectra from both phases, but is more pronounced in zircon. A small peak at 13.5 eV is similar in both phases. Also, zircon has a peak at 16.4 eV, while reidite has two at 15.3 and 17.8 eV (Table 1). The fine features between 30 and 40 eV in the VEELS (Fig. 2d) consist of two small peaks centered at ~33.5 and 35.5 eV in zircon, similar to those described by Jiang and Spence (2013) but absent in reidite. In zircon, the delayed maximum peak position is at about 41.1 eV with a shoulder at the right side, while in reidite it is at ca. 40 eV (Fig. 2d; Table 1).

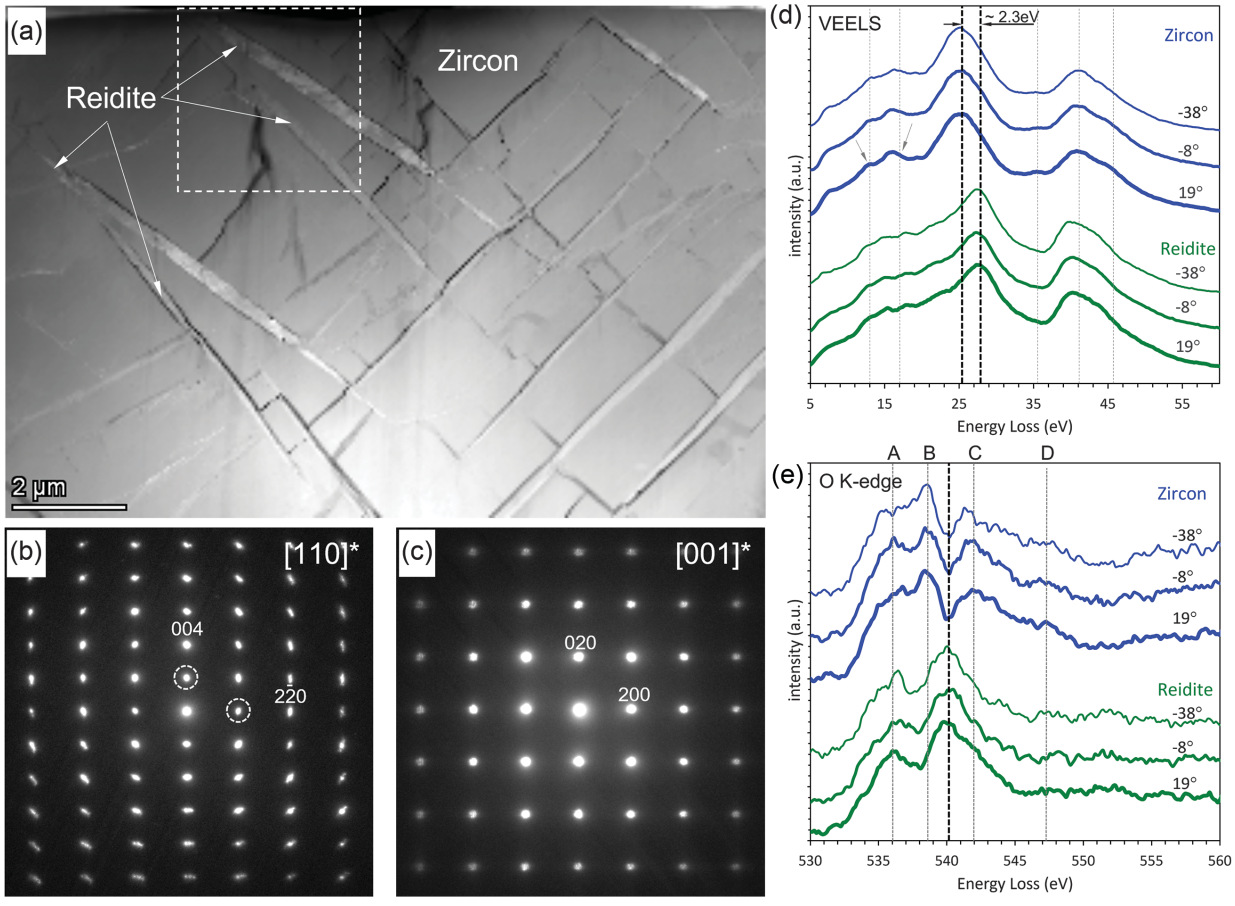

Figure 2. TEM images and analyses of FIB foil #7081. (**a**) HAADF image with identified lamellae of reidite (white arrows) and the fractured zircon. The dotted box shows the position of the phase map in Figure 3. (**b**) SAED pattern of reidite for the [110] crystallographic direction; forbidden spots are marked with dashed circles; (**c**) SAED pattern of zircon for the [001] direction. (**d**) Characteristic VEELS and (**e**) oxygen *K*-edge spectra of zircon (blue spectra) and reidite (green spectra) at different tilting angles (from bottom to top of each set represents the angles +19, −8, and −38°). Black dashed lines show the positions of the main peaks of zircon and reidite shifted by ~2.3 eV. The pronounced peaks in the near-edge region (535–555 eV) of the O *K*-edge ELNES of zircon are marked A–D after Jiang and Spence (2009).

Table 1. The list of features in the VEELS spectra of zircon and reidite, along with their assignments, and the band gap energies (E_g)

Zircon				Reidite			
Bulk	Surface	Interband	Assessment	Bulk	Surface	Interband	Assessment
~7.4	~7.4	>7	$O_2p \rightarrow Zr_4d$		~7.4	>7	$O_2p \rightarrow Zr_4d$
	12.2		Surface plasmon		12.2		Surface plasmon
13.5	14.6	14.0	$O_2p \rightarrow Si_3s$	~13	14	>7	$O_2p \rightarrow Si_3s$
16.4			Bulk plasmon	15.3			Bulk plasmon
				17.8			Bulk plasmon
	21.2		$O_2p \rightarrow Zr_5s$ O_2s-Op/Zr_4d		21.2		$O_2p \rightarrow Zr_5s$ O_2s-Op/Zr_4d
25.5			Bulk plasmon	27.6			Bulk plasmon
32.0–38.0			$O_2s \rightarrow Zr_5p$	32.0–38.0			$O_2s \rightarrow Zr_5p$
~41.1			$Zr_4p \rightarrow Zr_4d$	~40.7			$Zr_4p \rightarrow Zr_4d$

Note: The energy values are given in eV.

The oxygen *K*-edge spectra of the two phases also differ (Fig 2e). A single peak at about 540 eV in the oxygen *K*-edge of reidite is visible (Fig. 2e, black dashed line), while distinct peaks B and C occur in the oxygen *K*-edge of zircon. Also, there are two minor features between C and D peaks. The peaks A and B in the O *K*-edge EELS have been attributed to Zr-O interaction. Peak C in the O *K*-edge EELS appears due to the Si-O interaction, while peak D has both Si and Zr characteristics (Jiang and Spence 2009). The O *K*-edge ELNES of reidite shows a broad peak instead of two separate B and C peaks characteristics for zircon (Fig. 2e, thick dashed line), while peaks A and D in reidite both coincide with those in zircon. Interestingly, looking at the tilt series it becomes clear that the intensity of the A peak in zircon is dependent on the specimen tilt, while this effect is less pronounced in reidite. EELS spectra showing *K*- and *L*-edges of Si and *M*-edge of Zr are presented in Online Materials[1] Figure SI4. One can also notice differences between the spectra of zircon and reidite; however, the spectra are less suitable for mapping because of the poor signal-to-noise ratio at higher energy losses.

Using the EELS spectra, phase maps were produced (Fig. 3), where even thin (<30 nm) lamellae of reidite could be reliably identified. The PED from the same area (Figs. 3e–3f) did not reveal the thin lamellae of reidite entirely because of the large tilt (~14°) from the [110] direction and shadowing from the surrounding zircon. Moreover, the size of the parallel electron beam (2–3 nm) used to collect electron diffraction data is larger than the size of the converged beam used in STEM experiments (~0.1 nm). Crystallographic relationships between zircon and reidite show a complex dependency of reidite from parent zircon: c-axes of reidite form four clusters, roughly coincident with $<110>_z$ and $<100>_z$. Reidite axes show significant rotation (asterism).

Following the above-tested approach, we also mapped the more complex mineralogical composition of foil #7103, which consists of a mixture of granular zircon and irregular grains of reidite, with particles less than 1 μm in size and with a high defect density (Fig. 4; Online Materials[1] Fig. SI5). In addition, this sample contained fractures outlined by nanometer-sized *m*-ZrO_2 (baddeleyite, monoclinic), which could be identified using high-resolution HAADF imaging followed by fast Fourier transformation (FFT) analysis (Fig. 4b) and by comparing its EELS spectra with those published earlier (McComb et al. 1992;

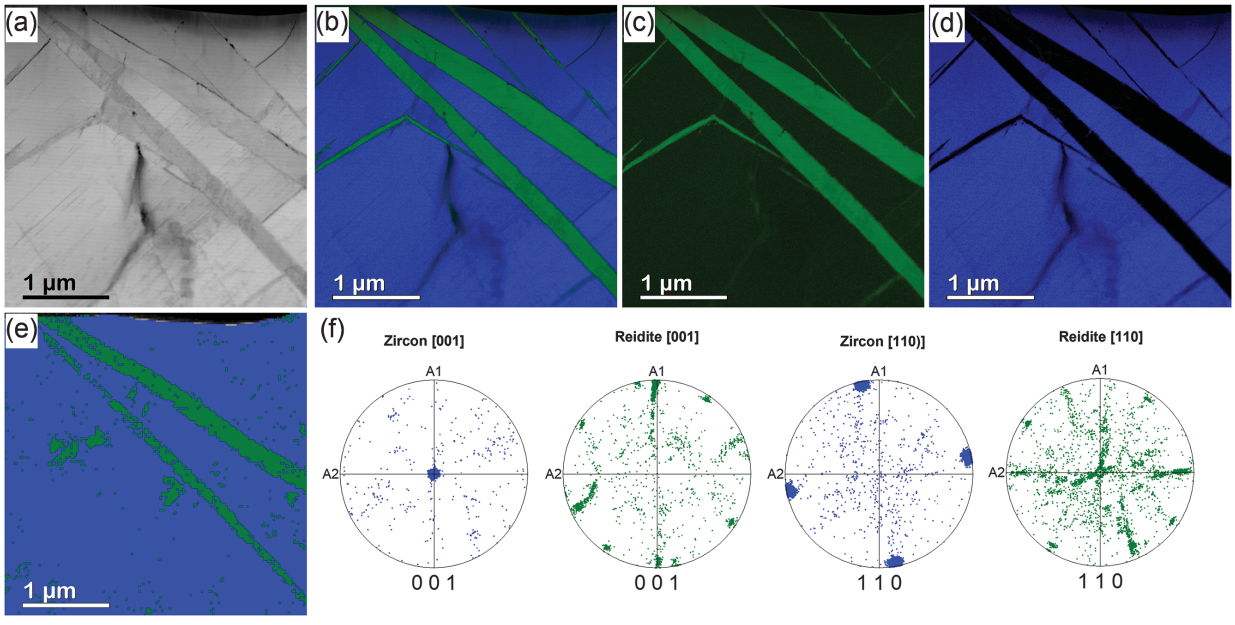

Figure 3. The detail marked as a dotted box in part of FIB foil #7081 shown in Figure 2a. (**a**) STEM image; (**b**) combined EELS map showing distribution of (**c**) reidite (green) and (**d**) zircon (blue); (**e**) combined image showing phase distribution as identified using PED; (**f**) corresponding pole figures of reidite and zircon for [001] and [110] orientations.

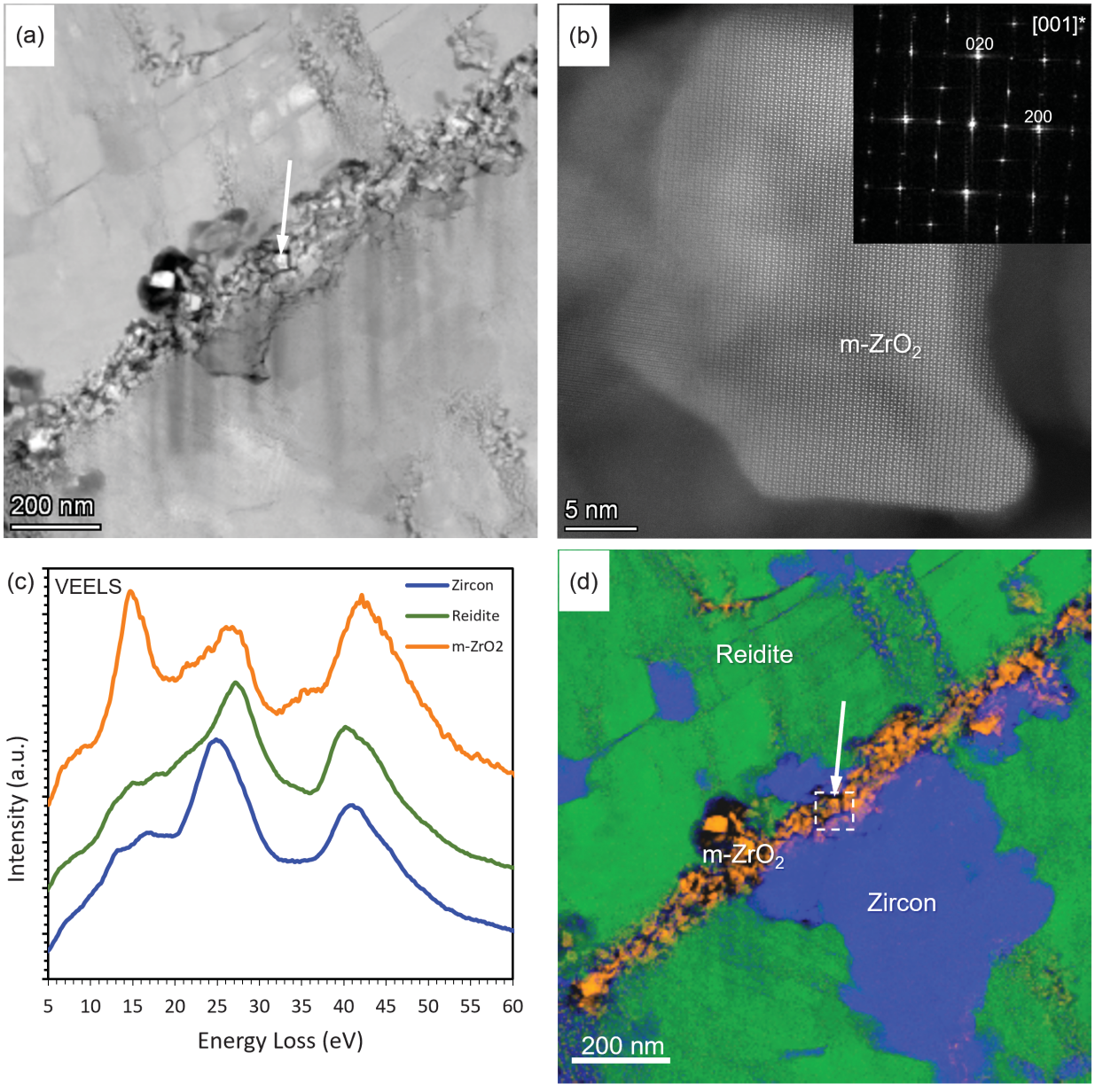

Figure 4. TEM results from FIB foil #7103. (**a**) HAADF image. A white arrow points at a single grain of *m*-ZrO_2 shown in (**b**); (**b**) HR-STEM image of *m*-ZrO_2 along [001]; (**c**) VEELS spectra of zircon, reidite, and the *m*-ZrO_2 phases collected over the imaged area shown in (**a**); (**d**) composite image showing the distribution of the three phases: reidite (green), zircon (blue), and *m*-ZrO_2 (orange).

Dash et al. 2004). In contrast to foil #7081, the textures and phases in foil #7103 are practically undistinguishable in the HAADF images alone. Thus, using representative spectra (Fig. 4c) of the different phases as explained above, we performed a MLLS fit to allow differentiation (Fig. 4d; Online Materials[1] Fig. SI5).

Two examples of small reidite and *m*-ZrO_2 inclusions in zircon are shown in Figures 5a and 6a, respectively. The inclusions were detected by VEELS mapping (Figs. 5b–5d, 6b, and 6c). Irregular nanometer-sized grains of reidite with sharp ragged boundaries are included in dense granular zircon matrix. The reidite inclusion in Figure 5 has sharp (Fig. 5e) and blurred (Fig. 5f) interfaces with surrounding zircon. The interface looks locally blurred due to the overlapping of both phases. It is worth noting that the true 2D shape of reidite inclusion in Figure 5a cannot be traced from the HAADF image. In contrast, the EELS maps allow for straightforward detection of such an inclusion even down to a nanometer scale.

In Figure 7, we show an image and corresponding VEELS and HL EELS spectrum of a lamellar grain with $ZrSiO_4$ composition but unusual radiating texture. Thin radiating lamellae 100–200 nm thick and several micrometers long have lobate boundaries, tapering tips, and pore space at the boundaries of adjacent lamellae. They are slightly misoriented from each other (<10°). The

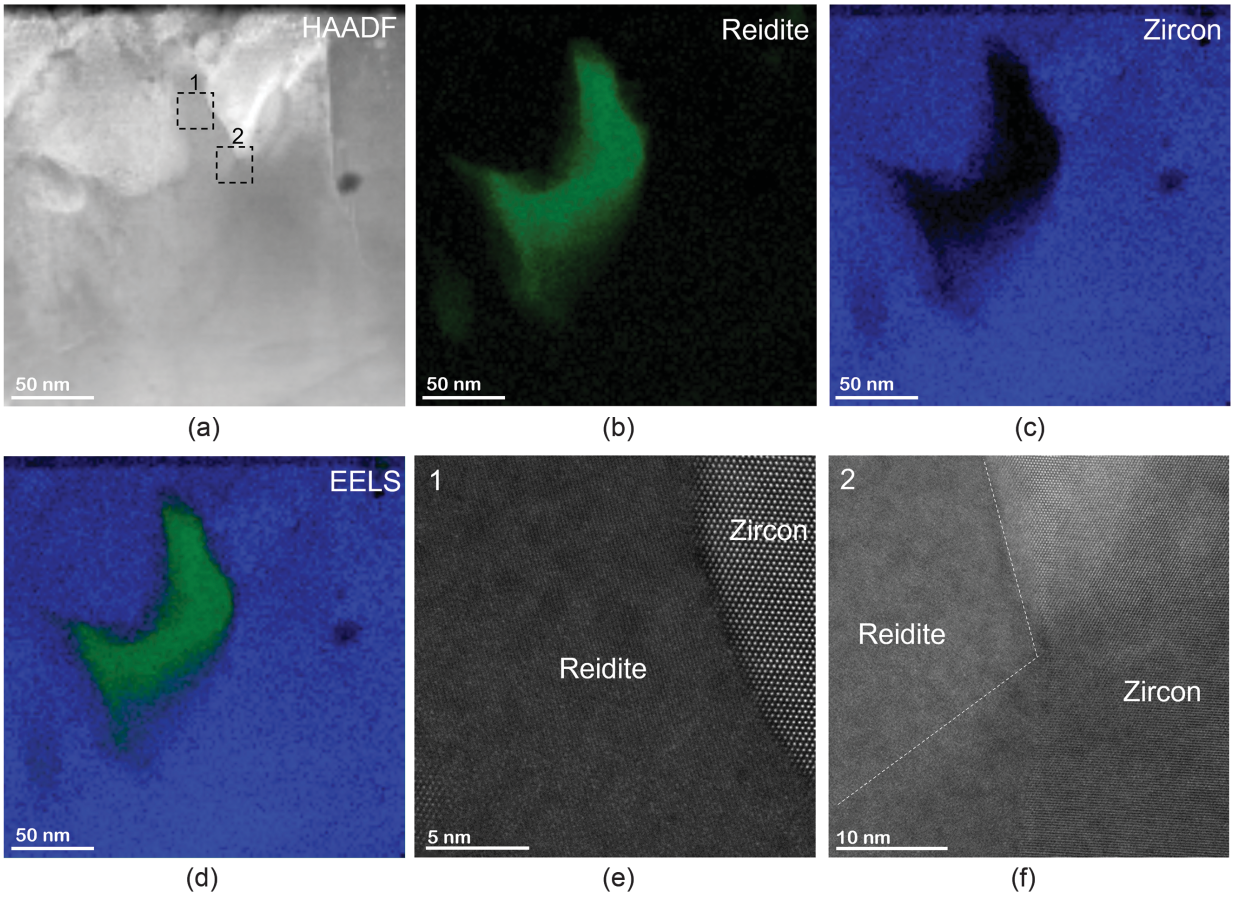

Figure 5. #7103 TEM specimen. (**a**) HAADF image of a reidite grain inside zircon matrix; corresponding phase maps of reidite (**b**) and zircon (**c**), respectively; (**d**) composed image of (**b**) and (**c**) maps; zoomed areas showing examples of a sharp (**e**) and blurred (**f**) reidite/zircon interfaces.

SAED was inconclusive to assign it to one of the two $ZrSiO_4$ polymorphs (Fig. 7a, inset). Therefore, we compared its VEELS (Fig. 7b) and O *K*-edge (Fig. 7c) spectra with those from the reference zircon (synthesized zircon), and shocked zircon and reidite materials. One can see that the VEELS and O *K*-edge spectra from the unknown aggregate differ from the spectra of zircon and reidite. While the positions of the main features in VEELS are similar to VEELS of zircon, the fine structure of the O *K*-edge is less visible. A more detailed study of crystalline structure using high-resolution STEM imaging (Fig. 7d) has revealed numerous voids of different sizes, overlapping areas between adjacent radial lamellae, and a high density of structural defects. We assume that the presence of these lattice distortions may be a reason for the lack of fine spectral features.

Discussion

Interpretations of observed textures

Using the proposed TEM-based mapping method, we demonstrated intricate features of two different textural relationships between zircon and reidite, which greatly facilitate interpretations of phase transition and mineral reactions.

The texture of foil #7081 shows defined planar reidite lamellae cutting the zircon grain in four directions with sharp boundaries without intermediate amorphous layers or other phases (Figs. 2–3; Online Materials[1] Fig. SI2). The zircon blocks have the same orientation (Figs. 3f–3g), suggesting that the zircon was a single grain that pre-existed the impact event and the reidite formation. The transverse relationships of oriented reidite lamellae in blocky zircon indicate shock-induced zircon-reidite transition (e.g., Reddy et al. 2015; Erickson et al. 2017). The high dislocation density in the reidite and cracks in the host zircon indicate changes in strain and volume associated with transformation (the reidite is approximately 10% denser). All four possible orientations of reidite (Erickson et al. 2017) are visible only in the EELS phase map (Fig. 2b), demonstrating the great advantage of the proposed method.

A more complicated texture in foil #7103 shows a dense polygranular zircon mass (Fig. 4d; Online Materials[1] Fig. SI5) with irregular inclusions of reidite (Fig. 5). The polygranular nature of zircon suggests that it is not original (preexisting), but recrystallized. Based on the empirical and experimental models, available in the literature, there are two scenarios by which this texture could have formed:

(1) As a result of zircon transformation to reidite and subsequent incomplete reversion from reidite back to zircon (Plan et al. 2021). Then the reidite inclusions (Online Materials[1] Fig. SI5) can be considered relics and would indicate at the direction of phase

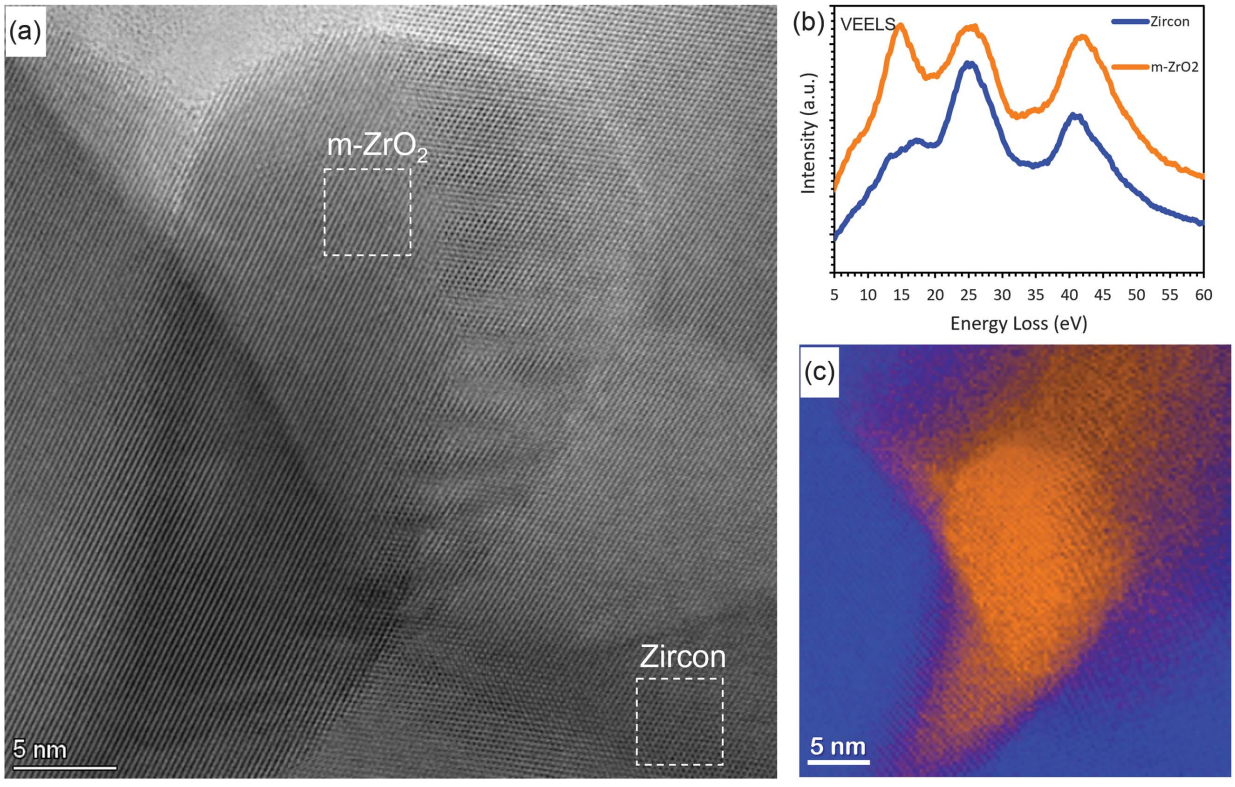

Figure 6. #7103 TEM specimen. (**a**) A bright-field high-resolution STEM image of *m*-ZrO_2 inclusion inside a small pore formed by zircon grains; (**b**) corresponding VEELS spectra collected from the positions marked with dashed squares in (**a**); (**c**) a corresponding phase distribution of *m*-ZrO_2 and zircon phases.

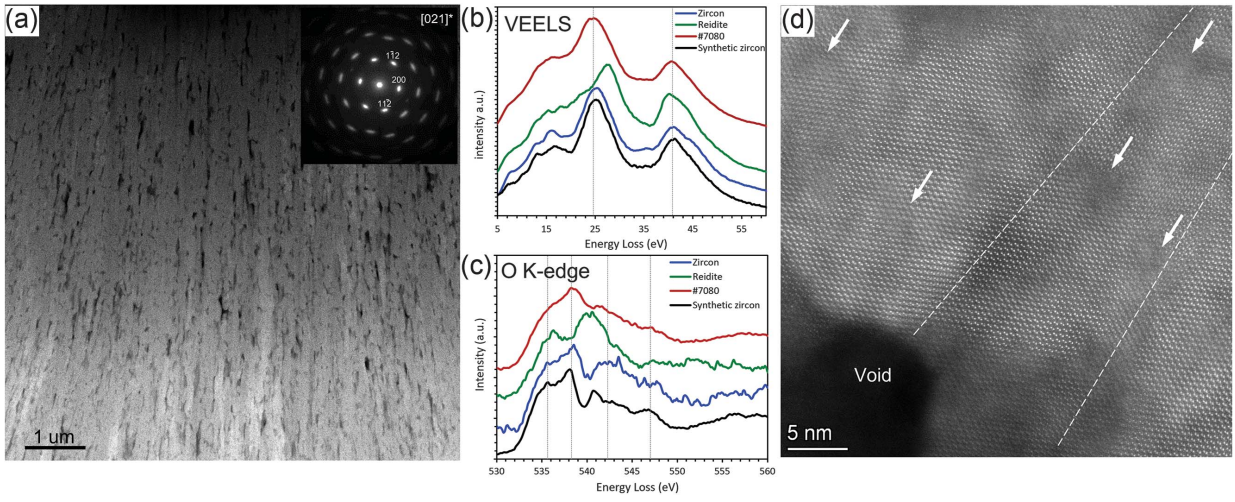

Figure 7. (**a**) HAADF image of TEM specimen #7080 and corresponding integrated nanobeam electron diffraction pattern (inset). Panels (**b**) and (**c**) correspond to VEELS and O *K*-edge spectra (red curves) as well as spectra of zircon (blue), reference zircon (black) and reidite (green) phases. The red curves are different from all three other phases, namely, it has no fine structure and only two broad main peaks visible. (**d**) HR STEM image of an area between two radiating lamellae. White dashed lines show the approximate overlapping area, which is terminated at a void; white arrows point out defects in the crystalline structure of zircon.

transition (reidite → zircon). The scenario (1) would imply the following: (a) preexisting zircon experienced high-pressure transition to reidite, followed by (b) reidite transformation to polygranular zircon (Online Materials[1] Fig SI5). Such texture was previously described and interpreted this way by Plan et al. (2021). However, this scenario does not clarify why domains composed of recrystallized zircon with reidite inclusions do not occur in the shape of lamellae if they form after reidite. It is

possible that granular—not lamellar—reidite had developed in an amorphous zircon core, as suggested by Erickson et al. (2017).

(2) As a result of an incomplete transformation of zircon to reidite through an intermediate elastic high-pressure low-symmetry (HPLS) phase (Mihailova et al. 2019; Stangarone et al. 2019). The latter experimentally demonstrated that static compression of zircon at above 20 GPa creates a mixture of the HPLS $ZrSiO_4$ phase (intermediate phase between zircon and reidite) and proper reidite. When the pressure is released, the HPLS phase transforms back to zircon. Hence, quenched samples were composed of a mixture of reidite and zircon, similar to what we observed in sample #7103. Hence, our Kara sample could be a natural equivalent of the experimental product of Stangarone et al. (2019).

In addition, small grains of *m*-ZrO_2 occur in arrays along fractures in foil #7103 (Figs. 4d; Online Materials[1] Fig. SI5). No silica or cubic zirconia were observed to support the high-temperature incongruent melting of $ZrSiO_4$, neither are there inclusions of ZrO_2 enclosed inside the zircon granules, opposite to the texture described by Kovaleva et al. (2021). Baddeleyite is most likely formed the latest, at the expense of $ZrSiO_4$ phases as a result of post-impact hydrothermally driven processes (Lewerentz et al. 2019).

Zircon aggregate sample #7080 with spherulitic shape and radiating lamellae of significantly damaged crystalline zircon (Fig. 7a) may be a result of:

(1) Complete (bulk) melting during shock loading (e.g., Takagi et al. 2022), followed by cooling to form radial lamellae. The position of zircon aggregate (sample KK21-21) at the boundary between a glass-rich domain and a lithic breccia domain (Online Materials[1] Fig. SI1) potentially supports this interpretation, as zircon could have crystallized from local melt upon contacting a colder breccia. However, no ZrO_2 or SiO_2 inclusions were found that often accompany high-temperature reactions involving zircon melting (e.g., Kovaleva et al. 2021, 2023; Wittmann et al. 2006). It would also be difficult to bulk-melt such a comparatively large volume of zircon.

(2) Transformation to HPLS phase and back to zircon upon pressure release (Stangarone et al. 2019). The lamellar structure of this sample resembles the lamellar nature of reidite inclusions in zircon, or aggregates that are almost completely transformed to reidite [Fig. 3; see multiple examples in Plan et al. (2021)]. Hence, the observed sample might represent an incomplete transition to massive reidite, which reverted back to zircon from the non-quenchable HPLS phase.

A variety of phases and their morphologies and structural damage found in shocked zircon aggregates suggests that we deal with various fixed snapshots of phase transformations determined by thermodynamic conditions and constrained by the local crystallo-chemical environment.

Broader geochemical and cosmochemical significance

Here, reidite is reported from the Kara impact structure, adding to the list of impact craters with this rare high-pressure polymorph. The presence of reidite indicates that the maximum shock pressure was at least 30 GPa (Kusaba et al. 1985). We also demonstrate the high-resolution appearance of texture resulting from the zircon-reidite and reidite-zircon phase transitions (Plan et al. 2021). More generally, our work provides a case study of how damaged and/or nano-sized phases can be resolved and studied with the level of details, unavailable for any other analytical methods. The presented workflow can be utilized for many other terrestrial and extraterrestrial samples, e.g., low volume samples obtained in sample return missions. Using the example of zircon-reidite aggregates, we show how phase distributions occurred due to mineral reactions and phase transitions can be studied at the atomic resolution.

Implications

Our data demonstrate that zircon and reidite are indeed characterized by distinct spectra in both low- and core-loss regions. This difference can be used to map their distribution in TEM specimens at very high spatial resolution and precision. Moreover, the fact that only low-loss spectra had to be collected for the maps provides another great advantage, as this means much shorter acquisition time (milliseconds vs. tens or hundreds of milliseconds for standard high-loss spectra per pixel or ED pattern per image in 4D-STEM experiments). This allows for minimizing the electron dose and thus the electron irradiation damage. Therefore, the presented EELS technique could also be applied to a variety of electron-beam-sensitive materials. Moreover, the procession time for PED data is much longer and crucially depends on the accuracy of the crystallographic information files that are used. Thus, our novel approach has great potential for phase mapping with unsurpassed spatial resolution for a series of geoscience applications.

Acknowledgments and funding

We thank J.M. Hanchar (Memorial University, Canada) for providing synthetic zircon for reference; the European Regional Development Fund and the State of Brandenburg for the Themis Z TEM (part of PISA). E.K. acknowledges the Alexander von Humboldt Foundation, and the European Union's Horizon 2020 research and innovation programme under grant agreement no. 101005611 (EXCITE) for Transnational Access conducted at the GFZ Helmholtz Centre for Geosciences (GFZ). The authors also acknowledge Liane Benning (GFZ), anonymous reviewers, and editors for their valuable comments.

References Cited

Badr N.N., Long F., Luo Y., Topping M., Béland L.K., Yao Z., Balogh L., and Daymond M.R. (2023) On potential core-shell morphologies of δ-hydride precipitates in zircaloy-2: A microstructural characterization approach by electron diffraction and energy-loss spectroscopy. Acta Materialia, 257, 119184.

Chen, C., Dai, M., Xu, C., Che, X., Dwyer, C., Luo, X., and Zhu, Y. (2024) Characteristic plasmon energies for 2D In_2Se_3 Phase Identification at Nanoscale. Nano Letters, 24, 1539–1543, https://doi.org/10.1021/acs.nanolett.3c04011.

Colliex, C. (2022) From early to present and future achievements of EELS in the TEM. The European Physical Journal Applied Physics, 97, 38, https://doi.org/10.1051/epjap/2022220012.

Dash, L.K., Vast, N., Baranek, P., Cheynet, M.-C., and Reining, L. (2004) Electronic structure and electron energy-loss spectroscopy of ZrO_2 zirconia. Physical Review B: Condensed Matter and Materials Physics, 70, 245116, https://doi.org/10.1103/PhysRevB.70.245116.

Egerton, R.F. (1996) Electron Energy-Loss Spectroscopy in the Electron Microscope, 2nd edition, 485 p. Plenum Press.

Erickson, T.M., Pearce, M.A., Reddy, S.M., Timms, N.E., Cavosie, A.J., Bourdet, J., Rickard, W.D.A., and Nemchin, A.A. (2017) Microstructural constraints on the mechanisms of the transformation to reidite in naturally shocked zircon. Contributions to Mineralogy and Petrology, 172, 6, https://doi.org/10.1007/s00410-016-1322-0.

Glass, B.P., Liu, S., and Leavens, P.B. (2002) Reidite: An impact-produced high-pressure polymorph of zircon found in marine sediments. American Mineralogist, 87, 562–565, https://doi.org/10.2138/am-2002-0420.

Gucsik, A., Koeberl, C., Brandstätter, F., Reimold, W.U., and Libowitzky, E. (2002) Cathodoluminescence, electron microscopy, and Raman spectroscopy of experimentally shock-metamorphosed zircon. Earth and Planetary Science Letters, 202, 495–509, https://doi.org/10.1016/S0012-821X(02)00754-9.

Gucsik, A., Koeberl, C., Brandstätter, F., Libowitzky, E., and Reimold, W.U. (2004) Cathodoluminescence, electron microscopy, and Raman spectroscopy of experimentally shock metamorphosed zircon crystals and naturally shocked zircon from the Ries impact crater. In H. Dypvik, M. Burchell, and P. Claeys, Eds., Cratering in Marine Environments and on Ice, 281–322. Springer-Verlag.

Jiang, N. and Spence, J.C.H. (2009) Interpretation of O *K*-edge EELS in zircon using a structural variation approach. Ultramicroscopy, 110, 89–93, https://doi.org/10.1016/j.ultramic.2009.09.012.

——— (2013) Valence electron energy-loss spectroscopy study of $ZrSiO_4$ and ZrO_2. Ultramicroscopy, 134, 68–76, https://doi.org/10.1016/j.ultramic.2013.06.021.

Johnson, D.W. and Spence, J.C.H. (1974) Determination of the single-scattering probability distribution from plural-scattering data. Journal of Physics D: Applied Physics, 7, 771–780, https://doi.org/10.1088/0022-3727/7/6/304.

Kenny, G.G., Öhman, T., Whitehouse, M.J., and Raitala, J. (2021) Zircon U–Pb dating of the Kara impact structure, Russia, indicates no role in Late Cretaceous mass extinctions. 52nd Lunar and Planetary Science Conference 2021, 1413 (LPI Contribution No. 2548).

Knittle, E. and Williams, Q. (1993) High-pressure Raman spectroscopy of $ZrSiO_4$: Observation of the zircon to scheelite transition at 300 K. American Mineralogist, 78, 245–252.

Kovaleva, E., Kusiak, M.A., Kenny, G.G., Whitehouse, M., Habler, G., Schreiber, A., and Wirth, R. (2021) Nano-scale investigation of granular neoblastic zircon, Vredefort impact structure, South Africa: Evidence for complete shock melting. Earth and Planetary Science Letters, 565, 116948, https://doi.org/10.1016/j.epsl.2021.116948.

Kovaleva, E., Helmy, H., Belkacim, S., Schreiber, A., Wilke, F.D.H., and Wirth, R. (2023) Libyan Desert Glass: New evidence for an extremely high-pressure-temperature impact event from nanostructural study. American Mineralogist, 108, 1906–1923, https://doi.org/10.2138/am-2022-8759.

Kramers, H.A. (1927) La diffusion de la lumiere par les atomes. In Atti del Congresso Internazionale dei Fisici, Transactions of Volta Centenary Congress Como. Bd. 2, 545–557.

Kronig, R. de L. (1926) On the theory of dispersion of X-rays. Journal of the Optical Society of America, 12, 547–556, https://doi.org/10.1364/JOSA.12.000547.

Kusaba, K., Syono, Y., Kikuchi, M., and Fukuoka, K. (1985) Shock behaviour of zircon: Phase transition to scheelite structure and decomposition. Earth and Planetary Science Letters, 72, 433–439, https://doi.org/10.1016/0012-821X(85)90064-0.

Leapman, R.D. and Swyt, C.R. (1988) Separation of overlapping core edges in electron energy loss spectra by multiple-least-squares fitting. Ultramicroscopy, 26, 393–403, https://doi.org/10.1016/0304-3991(88)90239-2.

Leroux, H., Reimold, W.U., Koeberl, C., Hornemann, U., and Doukhan, J.-C. (1999) Experimental shock deformation in zircon: A transmission electron microscopic study. Earth and Planetary Science Letters, 169, 291–301, https://doi.org/10.1016/S0012-821X(99)00082-5.

Lewerentz, A., Harlov, D.E., Scherstén, A., and Whitehouse, M.J. (2019) Baddeleyite formation in zircon by Ca-bearing fluids in silica-saturated systems in nature and experiment: Resetting of the U–Pb geochronometer. Contributions to Mineralogy and Petrology, 174, 64, https://doi.org/10.1007/s00410-019-1600-8.

Liang, R.-Z., Babics, M., Savikhin, V., Zhang, W., Le Corre, V.M., Lopatin, S., Kan, Z., Firdaus, Y., Liu, S., McCulloch, I., and others. (2018) Carrier transport and recombination in efficient "all-small-molecule" solar cells with the nonfullerene acceptor IDTBR. Advanced Energy Materials, 8, 1800264, https://doi.org/10.1002/aenm.201800264.

Masaitis, V.L. (1999) Impact structures of northeastern Eurasia: The territories of Russia and adjacent countries. Meteoritics & Planetary Science, 34, 691–711, https://doi.org/10.1111/j.1945-5100.1999.tb01381.x.

Mihailova B., Waeselmann N., Stangarone C., Angel R.J., Prencipe M., and Alvaro M. (2019) The pressure-induced phase transition(s) of $ZrSiO_4$: revised, Physics and Chemistry of Minerals, 46, 807–814.

McComb, D.W., Brydson, R., Hansen, P.L., and Payne, R.S. (1992) Qualitative interpretation of electron energy-loss near-edge structure in natural zircon. Journal of Physics Condensed Matter, 4, 8363–8374, https://doi.org/10.1088/0953-8984/4/43/011.

Mu, X., Kobler A., Wang, D., Chakravadhanula, V.S.K., Schlabach, S., Szabó, D.V., Norby, P., and Kübel, C. (2016) Comprehensive analysis of TEM methods for $LiFePO_4$/$FePO_4$ phase mapping: spectroscopic techniques (EFTEM, STEM-EELS) and STEM diffraction techniques (ACOM-TEM). Ultramicroscopy, 170, 10–18.

Mundet, B., Domínguez, C., Fowlie, J., Gibert, M., Triscone, J.-M., and Alexander, D.T.L. (2021) Near-atomic-scale mapping of electronic phases in rare earth nickelate superlattices. Nano Letters, 21, 2436–2443, https://doi.org/10.1021/acs.nanolett.0c04538.

Plan, A., Kenny, G.G., Erickson, T.M., Lindgren, P., Alwmark, C., Holm-Alwmark, S., Lambert, P., Scherstén, A., and Söderlund, U. (2021) Exceptional preservation of reidite in the Rochechouart impact structure, France: New insights into shock deformation and phase transition of zircon. Meteoritics & Planetary Science, 56, 1795–1828, https://doi.org/10.1111/maps.13723.

Reddy, S.M., Johnson, T.E., Fischer, S., Rickard, W.D.A., and Taylor, R.J.M. (2015) Precambrian reidite discovered in shocked zircon from the Stac Fada impactite, Scotland. Geology, 43, 899–902, https://doi.org/10.1130/G37066.1.

Rossner, C., Tang, Q., Müller, M., and Kothleitner, G. (2018) Phase separation in mixed polymer brushes on nanoparticle surfaces enables the generation of anisotropic nanoarchitectures. Soft Matter, 14, 4551–4557, https://doi.org/10.1039/C8SM00545A.

Stangarone, C., Angel, R.J., Prencipe, M., Mihailova, B., and Alvaro, M. (2019) New insights into the zircon-reidite phase transition. American Mineralogist, 104, 830–837, https://doi.org/10.2138/am-2019-6827.

Takagi, S., Ichiyanagi, K., Kyono, A., Kawai, N., Nozawa, S., Ozaki, N., Seto, Y., Okuchi, T., Nitta, S., Okada, S., and others. (2022) Phase transition and melting in zircon by nanosecond shock loading. Physics and Chemistry of Minerals, 49, 8, https://doi.org/10.1007/s00269-022-01184-8.

Trieloff, M., Deutsch, A., and Jessberger, E.K. (1998) The age of the Kara Impact structure, Russia. Meteoritics & Planetary Science, 33, 361–372, https://doi.org/10.1111/j.1945-5100.1998.tb01640.x.

Wittmann, A., Kenkmann, T., Schmitt, R.T., and Stöffler, D. (2006) Shock-metamorphosed zircon in terrestrial impact craters. Meteoritics & Planetary Science, 41, 433–454, https://doi.org/10.1111/j.1945-5100.2006.tb00472.x.

Xing, W., Lin, Y., Zhang, C., Zhang, M., Hu, S., Hofmann, B.A., Sekine T., Xiao L., and Gu L. (2020) Discovery of reidite in the lunar meteorite Sayh al Uhaymir 169. Geophysical Research Letters, 47, e2020GL089583.

Yakovlev, S. and Libera, M. (2008) Dose-limited spectroscopic imaging of soft materials by low-loss EELS in the scanning transmission electron microscope. Micron, 39, 734–740.

Yeh, Y.-W., Singh, S., Cheng, G., Yao, N., Rabe, K.M., Vanderbilt, D., Batson, P.E., Pan, L., Xu, G., and Xu, S. (2023) Differentiating the bonding states in calcium carbonate polymorphs by low-loss electron-energy-loss spectroscopy. Acta Materialia, 257, 119191, https://doi.org/10.1016/j.actamat.2023.119191.

Zhao, J., Zhang, X., Xiao, L., Cavosie, A.J., Timms, N.E., Nemchin, A., Xiao, Z., Hu, W., Chang, Y., Shu, J., and others. (2024) Nanoscale constraints on the nucleation and evolution of granular zircon from reidite in impactites at the Chicxulub impact structure. Earth and Planetary Science Letters, 626, 118507, https://doi.org/10.1016/j.epsl.2023.118507.

Manuscript received May 7, 2024
Manuscript accepted February 2, 2025
Accepted manuscript online February 19, 2025
Manuscript Handled by Bradley T. De Gregorio

Endnotes:

[1]Deposit item AM-25-119455. Online Materials are free to all readers. Go online, via the table of contents or article view, and find the tab or link for supplemental materials.